

9

Particle identification

It is impossible to trap modern physics into predicting anything with perfect determinism because it deals with probabilities from the outset.

Sir Arthur Eddington

One of the tasks of particle detectors is, apart from measuring characteristic values like momentum and energy, to determine the identity of particles. This implies the determination of the mass and charge of a particle. In general, this is achieved by combining information from several detectors.

For example, the radius of curvature ρ of a charged particle of mass m_0 in a magnetic field supplies information on the momentum p and the charge z via the relation

$$\rho \propto \frac{p}{z} = \frac{\gamma m_0 \beta c}{z} . \quad (9.1)$$

The velocity $\beta = v/c$ can be obtained by time-of-flight measurements using

$$\tau \propto \frac{1}{\beta} . \quad (9.2)$$

The determination of the energy loss by ionisation and excitation can approximately be described by, see Chap. 1,

$$-\frac{dE}{dx} \propto \frac{z^2}{\beta^2} \ln(a\gamma\beta) , \quad (9.3)$$

where a is a material-dependent constant. An energy measurement yields

$$E_{\text{kin}} = (\gamma - 1)m_0c^2 , \quad (9.4)$$

since normally only the kinetic energy rather than the total energy is measured.

Equations (9.1) to (9.4) contain three unknown quantities, namely m_0, β and z ; the Lorentz factor γ is related to the velocity β according to $\gamma = 1/\sqrt{1 - \beta^2}$. Three of the above-mentioned four measurements are in principle sufficient to positively identify a particle. In the field of elementary particle physics one mostly deals with singly charged particles ($z = 1$). In this case, two different measurements are sufficient to determine the particle's identity. For particles of high energy, however, the determination of the velocity does not provide sufficient information, since for all relativistic particles, independent of their mass, β is very close to 1 and therefore cannot discriminate between particles of different mass.

In large experiments all systems of a general-purpose detector contribute to *particle identification* by providing relevant parameters which are combined to joint likelihood functions (see Chap. 15). These functions are used as criteria to identify and distinguish different particles. In practice, the identification is never perfect. Let us assume that particles of type I should be selected in the presence of high background of particles of type II (pion versus kaon, electron versus hadron, etc.). Then any selection criterion is characterised by the identification efficiency ε_{id} for type I at certain probability p_{mis} to misidentify the particle of type II as type I.

9.1 Charged-particle identification

A typical task of experimental particle physics is to identify a charged particle when its momentum is measured by a magnetic spectrometer.

9.1.1 Time-of-flight counters

A direct way to determine the particle velocity is to measure its time of flight (TOF) between two points separated by a distance L . These two points can be defined by two counters providing 'start' and 'stop' signals or by the moment of particle production and a stop counter. In the latter case the 'start' signal synchronised with the beam-beam or beam-target collision can be produced by the accelerator system. A more detailed review of TOF detectors in high-energy particle experiments can be found in [1, 2].

Two particles of mass m_1 and m_2 have for the same momentum and flight distance L the time-of-flight difference

$$\Delta t = L \left(\frac{1}{v_1} - \frac{1}{v_2} \right) = \frac{L}{c} \left(\frac{1}{\beta_1} - \frac{1}{\beta_2} \right) . \quad (9.5)$$

Using $pc = \beta E$ we obtain

$$\Delta t = \frac{L}{pc^2}(E_1 - E_2) = \frac{L}{pc^2} \left(\sqrt{p^2c^2 + m_1^2c^4} - \sqrt{p^2c^2 + m_2^2c^4} \right) . \quad (9.6)$$

Since in this case $p^2c^2 \gg m_{1,2}^2c^4$, the expansion of the square roots leads to

$$\Delta t = \frac{Lc}{2p^2}(m_1^2 - m_2^2) . \quad (9.7)$$

Suppose that for a mass separation a significance of $\Delta t = 4\sigma_t$ is demanded. That is, a time-of-flight difference four times the time resolution is required. In this case a pion/kaon separation can be achieved up to momenta of 1 GeV/c for a flight distance of 1 m and a time resolution of $\sigma_t = 100$ ps, which can be obtained with, e.g., scintillation counters [1, 2]. For higher momenta the time-of-flight systems become increasingly long since $\Delta t \propto 1/p^2$.

At present the most developed and widely used technique for *TOF measurements* in high energy physics is based on plastic scintillation counters with PM-tube readout (see Sect. 5.4). A typical layout is shown in Fig. 9.1. The beam-crossing signal related to the interaction point starts the TDC (time-to-digital converter). The signal from the PM anode, which reads out the ‘stop’ counter, is fed to a discriminator, a device which generates a standard (logic) output pulse when the input pulse exceeds a certain threshold. The discriminator output is connected to the ‘stop’ input of the TDC. The signal magnitude is measured by an ADC (amplitude-to-digital converter). Since the moment of threshold crossing usually depends on the pulse height, a measurement of this value helps to make corrections in the off-line data processing.

The time resolution can be approximated by the formula

$$\sigma_t = \sqrt{\frac{\sigma_{sc}^2 + \sigma_l^2 + \sigma_{PM}^2}{N_{eff}} + \sigma_{el}^2} , \quad (9.8)$$

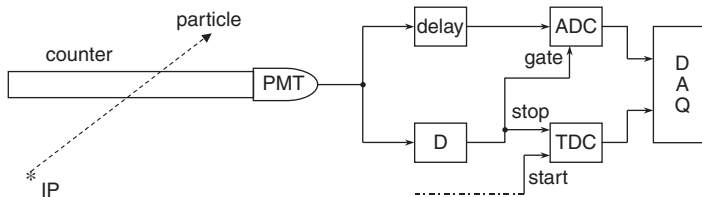


Fig. 9.1. The principle of time-of-flight measurements: IP – interaction point, D – discriminator, TDC – time-to-digital converter, ADC – amplitude-to-digital converter, DAQ – data-acquisition system.

where σ_{sc} is the contribution of the light-flash duration, σ_1 the variation of the travel time due to different particle impact points and various emission angles of scintillation photons, σ_{PM} the photoelectrons' transit-time spread, N_{eff} the effective number of photoelectrons produced at the PM photocathode, and σ_{el} is the electronics contribution to the time resolution. The quantity N_{eff} is usually smaller than the total number of photoelectrons since some of them will arrive too late at the first dynode of the PM tube due to large emission angles to be useful for signal generation. The total photoelectron number is given by Eq. (5.58), where the deposited energy E_{dep} is proportional to the scintillator thickness. For large-size counters the light attenuation length becomes crucial to obtain a large N_{eff} .

For long counters the measured time depends on the point x where the particle crosses the counter,

$$t_m = t_0 + \frac{x}{v_{eff}} \quad , \quad (9.9)$$

where v_{eff} is the effective light speed in the scintillator. To compensate this dependence the scintillation bar is viewed from both edges. Then the average of two measured times, $(t_1 + t_2)/2$, is – at least partially – compensated. Further corrections can be applied taking into account the impact coordinates provided by the tracking system.

The time resolution achieved for counters of 2–3 m length and $(5-10) \times (2-5) \text{ cm}^2$ cross section is about 100 ps [3–6]. Even better resolutions, 40–60 ps, were reported for the TOF counters of the GlueX experiment [7].

Very promising results were reported recently for TOF counters based on Cherenkov-light detection [8, 9]. The light flash in this case is extremely short. Moreover, the variations in the photon path length can be kept small in comparison to the scintillation light as all Cherenkov photons are emitted at the same angle to the particle trajectory. To demonstrate this, $4 \times 4 \times 1 \text{ cm}^3$ glass plates viewed by a microchannel plate (MCP) PM tube (see Sect. 5.5) were used in [10]. A time resolution of about 6 ps was achieved.

Another device for time measurement is the *planar spark counter*. Planar spark counters consist of two planar electrodes to which a constant voltage exceeding the static breakdown voltage at normal pressure is applied. The chambers are normally operated with slight overpressure. Consequently, the planar spark counter is essentially a spark chamber which is not triggered. Just as in a spark chamber, the ionisation of a charged particle, which has passed through the chamber, causes an avalanche, which develops into a conducting plasma channel connecting the electrodes. The rapidly increasing anode current can be used to generate a voltage signal of very short rise time via a resistor. This voltage pulse

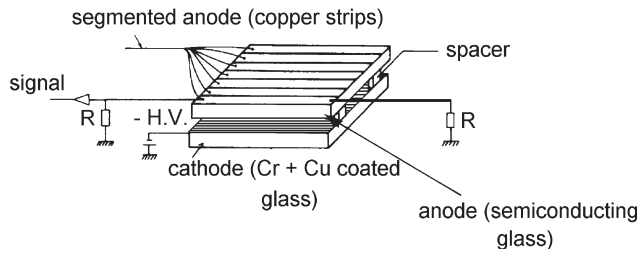


Fig. 9.2. Working principle of a planar spark counter [11, 12]. In many cases the anode is either coated with a semiconducting material or with a material of high specific bulk resistivity.

can serve as a very precise timing signal for the arrival time of a charged particle in the spark counter.

Figure 9.2 shows the working principle of a planar spark counter [1, 11, 12]. If metallic electrodes are used, the total capacitance of the chamber will be discharged in one spark. This may lead to damages of the metallic surface and also causes a low multitrack efficiency. If, however, the electrodes are made from a material with high specific bulk resistivity [13, 14], only a small part of the electrode area will be discharged via the sparks (Pestov counters). These do not cause surface damage because of the reduced current in the spark. A high multitrack efficiency is also guaranteed in this way. In addition to determining the arrival time of charged particles, the chamber also allows a spatial resolution if the anode is segmented. Noble gases with quenchers which suppress secondary spark formation are commonly used as gas filling.

Planar spark counters provide excellent time resolution ($\sigma_t \leq 30$ ps) if properly constructed [15]. This, however, requires narrow electrode gaps on the order of $100\ \mu\text{m}$. The production of large-area spark counters, therefore, requires very precise machining to guarantee parallel electrodes with high surface quality.

Planar spark counters can also be operated at lower gas amplifications, and are then referred to as *resistive plate chambers* (RPCs), if, for example, instead of semiconducting electrode materials, graphite-covered glass plates are used. These chambers are most commonly operated in the streamer or in the avalanche mode [1, 16, 17]. Instead of graphite-covered glass plates other materials with suitable surface resistivity like Bakelite, a synthetic resin, can also be used. These resistive plate chambers also supply very fast signals and can – just as scintillation counters – be used for triggering with high time resolution. If the electrodes of the resistive plate chambers are segmented, they may also provide an excellent position resolution.

Planar spark counters and resistive plate chambers generally do not permit high counting rates. If the gas amplification is further reduced to values around 10^5 , neither sparks nor streamers can develop. This mode of operation characterises a *parallel-plate avalanche chamber* (PPAC or PPC) [18–21]. These parallel-plate avalanche chambers, with typical electrode distances on the order of 1 mm, also exhibit a high time resolution (≈ 500 ps) and, if they are operated in the proportional mode, have as well an excellent energy resolution [22]. An additional advantage of parallel-plate avalanche chambers, compared to spark counters and resistive plate chambers, is that they can be operated at high counting rates because of the low gas amplification involved.

All these chamber types have in common that they provide excellent timing resolution due to the small electrode gaps. The present status of the counters with localised discharge and its applications is reviewed in [23].

9.1.2 Identification by ionisation losses

Since the specific ionisation energy loss depends on the particle energy, this can be used for identification (see Chap. 1). The average energy loss of electrons, muons, pions, kaons and protons in the momentum range between $0.1 \text{ GeV}/c$ and $100 \text{ GeV}/c$ in a 1 cm layer of argon–methane (80%:20%) is shown in Fig. 9.3 [24, 25]. It is immediately clear that a muon/pion separation on the basis of an energy-loss measurement is practically impossible, because they are too close in mass. However, a $\pi/K/p$ separation should be achievable. The logarithmic rise of the energy loss in gases ($\propto \ln \gamma$, see Eq. (1.11)) amounts to 50% up to 60% compared to the energy loss of minimum-ionising particles at a pressure of 1 atm [25, 26].

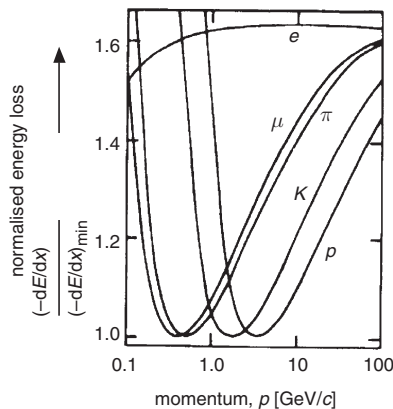


Fig. 9.3. Average energy loss of electrons, muons, pions, kaons and protons, normalised to the minimum-ionising value [24].

It should be noted that the relativistic rise of dE/dx is almost completely suppressed in solid-state materials by the density effect. Thus, solid-state detectors, like semiconductors or scintillators, can be used for dE/dx particle identification only in the low β range.

The key problem of *particle identification* by dE/dx is the fluctuation of the ionisation losses (see Chap. 1). A typical energy-loss distribution of 50 GeV/ c pions and kaons in a layer of 1 cm argon–methane mixture (80%:20%) is sketched in Fig. 9.4 (left). The width of this distribution (FWHM) for gaseous media is in the range of 40%–100%. A real distribution measured for 3 GeV electrons in a thin-gap multiwire chamber is shown in Fig. 9.4 (right) [27]. To improve the resolution, multiple dE/dx measurements for the particles are used.

However, asymmetric energy-loss distributions with extended high-energy-loss tails render the direct averaging of the measured values inefficient. The origin of such long tails is caused by single δ electrons which can take away an energy ϵ_δ that is much larger than the average ionisation loss. The widely used ‘*truncated mean*’ method implies an exclusion of a certain part (usually 30%–60%) of all individual energy-loss measurements with the largest values and averaging

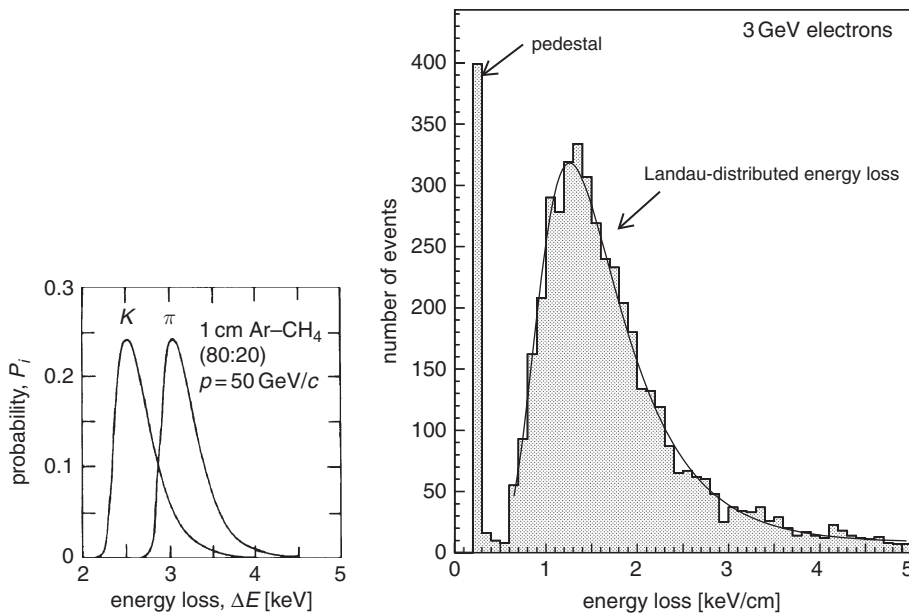


Fig. 9.4. Energy-loss distribution of 50 GeV/ c pions and kaons in a layer of 1 cm argon and methane (left). The distribution measured for 3 GeV electrons in a thin-gap multiwire chamber (right) [27]. See also the discussion of this figure in Sect. 1.1.

over the remaining ones. This method excludes high energy transfers caused by the occasional production of energetic δ electrons. Sometimes also the lowest dE/dx measurements are discarded (typically 10%) to aim for a Gaussian-like energy-loss distribution. With about 100 dE/dx measurements energy-loss resolutions of

$$\frac{\sigma(dE/dx)}{(dE/dx)} \approx (2-3)\% \quad (9.10)$$

for pions, kaons and protons of 50 GeV can be achieved [28].

The resolution can be improved by increasing the number N of individual measurements according to $1/\sqrt{N}$, which means, to improve the dE/dx resolution by a factor of two, one has to take four times as many dE/dx measurements. For a fixed total length of a detector, however, there exists an optimum number of measurements. If the detector is subdivided in too many dE/dx layers, the energy loss per layer will eventually become too small, thereby increasing its fluctuation. Typically, the dE/dx resolution for the drift chambers used in high energy physics experiments is in the range from 3% to 10% [2, 26].

The resolution should also improve with increasing gas pressure in the detector. One must, however, be careful not to increase the pressure too much, otherwise the logarithmic rise of the energy loss, which is a basis for particle identification, will be reduced by the onset of the density effect. The increase of the energy loss compared to the minimum of ionisation at 1 atm amounts to about 55%. For 7 atm it is reduced to 30%.

An alternative, more sophisticated method compared to the use of the truncated mean of a large number of energy-loss samples, which also provides more accurate results, is based on likelihood functions. Let $p_\pi(A)$ be the probability density function (PDF) for the magnitude of a signal produced by a pion in the single sensitive layer. Each particle yields a set of $A_i (i = 1, 2, \dots, N)$ signals. Then the pion likelihood function can be built as

$$L_\pi = \prod_{i=1}^N p_\pi(A_i) . \quad (9.11)$$

Of course, this expression is valid under the assumption that measurements in different layers are statistically independent. In general, the PDF for different layers can be different. Correspondingly, a kaon likelihood function for the same set of signals is

$$L_K = \prod_{i=1}^N p_K(A_i) . \quad (9.12)$$

Then the most efficient parameter to choose one of the two alternative hypotheses on the type of the particle (pion or kaon) is a likelihood ratio as it was suggested by Neyman and Pearson (see, e.g., [29] for details):

$$R_L = \frac{L_\pi}{L_\pi + L_K} . \quad (9.13)$$

The likelihood-ratio method is rather time consuming, but it uses all available information and provides better results compared to the truncated-mean method.

Figure 9.5 shows the results of energy-loss measurements in a mixed particle beam [24]. This figure very clearly shows that the method of particle separation by dE/dx sampling only works either below the minimum of ionisation ($p < 1 \text{ GeV}/c$) or in the relativistic-rise region. The identification by the ‘truncated mean’ method in various momentum ranges is illustrated by Fig. 9.6. These results were obtained with the ALEPH TPC which produced up to 344 measurements per track. A ‘60% truncated mean’ was used providing about 4% for the resolution $\sigma(dE/dx)/(dE/dx)$ [30].

9.1.3 Identification using Cherenkov radiation

The main principles of Cherenkov counters are described in Sect. 5.6. This kind of device is widely used for particle identification in high energy physics experiments. The gaseous threshold counters are often exploited

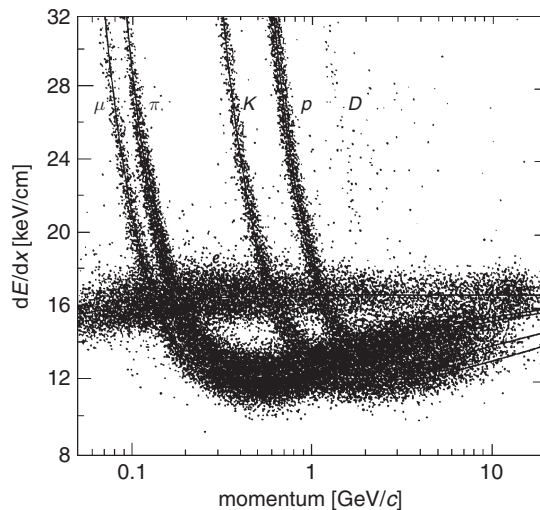


Fig. 9.5. Energy-loss measurements in a mixed particle beam [24].

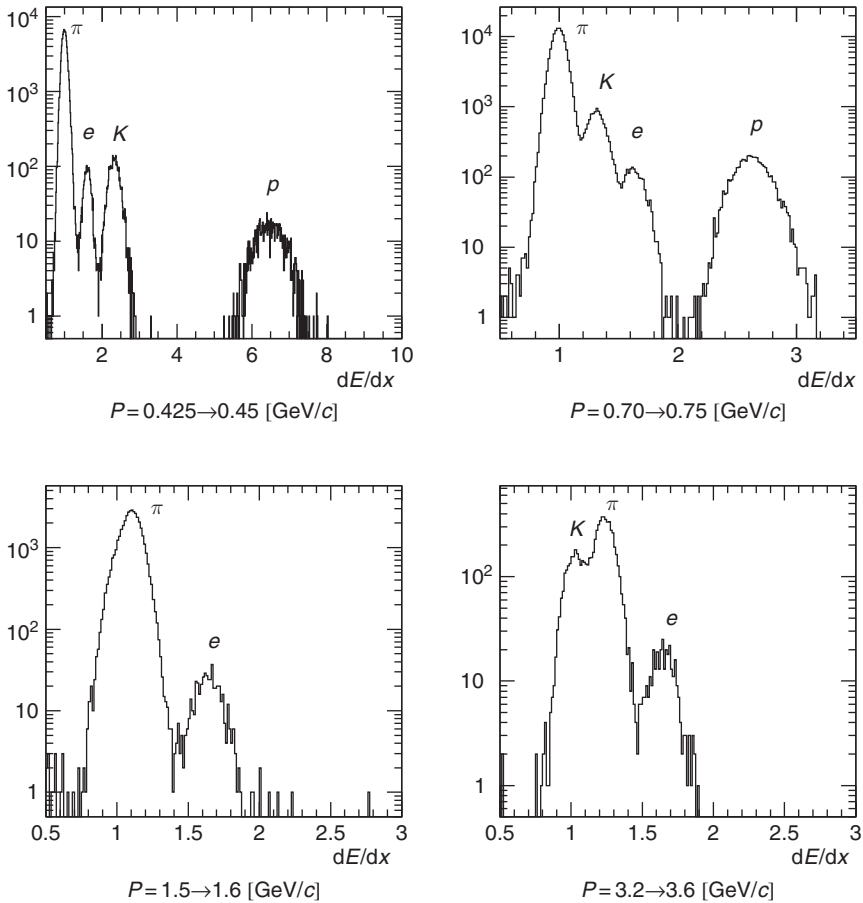


Fig. 9.6. Truncated energy-loss distributions for electrons, pions, kaons and protons in the ALEPH time-projection chamber in various momentum ranges [31].

in fixed-target experiments (see, e.g., [32]). Aerogel-based multielement systems (see Sect. 5.6) are used for detectors with 4π geometry. One of such systems is described in detail in Chap. 13. Other examples are considered in [33–35]. Counters of this type can provide a pion/kaon separation up to 2.5–3 GeV.

Although the differential Cherenkov counters provide better particle identification, conventional differential counters cannot be used in storage-ring experiments where particles can be produced over the full solid angle. This is the domain of RICH counters (*Ring Imaging Cherenkov counters*) [36, 37]. An example of the RICH design is presented in Fig. 9.7 [38]. In this example a spherical mirror of radius R_S , whose centre of curvature coincides with the interaction point, projects the cone of Cherenkov light

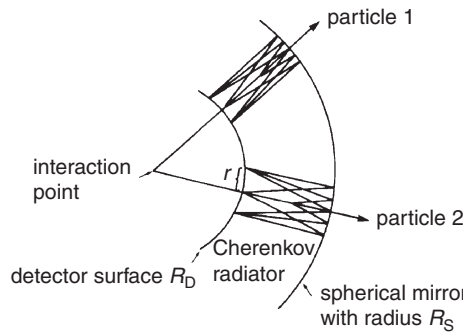


Fig. 9.7. Working principle of a RICH counter [38].

produced in the radiator onto a ring on the surface of a spherical detector of radius R_D (see Fig. 9.7).

The radiator fills the volume between the spherical surfaces with radii R_S and R_D . In general, one takes $R_D = R_S/2$, since the focal length f of a spherical mirror is $R_S/2$. Because all Cherenkov photons are emitted at the same angle θ_c with respect to the particle trajectory pointing away from the sphere centre, all of them will be focussed to the thin detector ring on the inner sphere. One can easily calculate the radius of the Cherenkov ring on the detector surface,

$$r = f \cdot \theta_c = \frac{R_S}{2} \cdot \theta_c . \quad (9.14)$$

The measurement of r allows one to determine the particle velocity via

$$\cos \theta_c = \frac{1}{n\beta} \rightarrow \beta = \frac{1}{n \cos \left(\frac{2r}{R_S} \right)} . \quad (9.15)$$

It should be noted that many other designs exist, for example [39–43]. As Cherenkov radiators, heavy gases, like freons, or UV-transparent crystals, for example CaF_2 or LiF , are typically used.

If the momentum of the charged particle is already known, e.g. by magnetic deflection, then the particle can be identified (i.e. its mass m_0 determined) from the size of the Cherenkov ring, r . From Eq. (9.15) the measurement of r yields the particle velocity β , and by use of the relation

$$p = \gamma m_0 \beta c = \frac{m_0 c \beta}{\sqrt{1 - \beta^2}} \quad (9.16)$$

the mass m_0 can be determined.

The most crucial aspect of RICH counters is the detection of Cherenkov photons with high efficiency on the large detector surface. Since one is not only interested in detecting photons, but also in measuring their coordinates, a position-sensitive detector is necessary. Multiwire proportional chambers, with an admixture of a photosensitive vapour in the counter gas, are a quite popular solution. The first generation of the RICH detectors used vapour additions such as triethylamine (TEA: $(C_2H_5)_3N$) with an ionisation energy of 7.5 eV and tetrakis-dimethylaminoethylene (TMAE: $[(CH_3)_2N]_2C = C_5H_{12}N_2$; $E_{ion} = 5.4$ eV), which yields 5–10 photoelectrons per ring. TEA is sensitive in the photon energy range from 7.5 eV to 9 eV which requires a crystal window like CaF_2 or LiF , while TMAE photo-ionisation occurs by photons of 5.5 eV to 7.5 eV allowing the work with quartz windows. Figure 9.8 shows the pion/kaon separation in a RICH counter at 200 GeV/c. For the same momentum kaons are slower

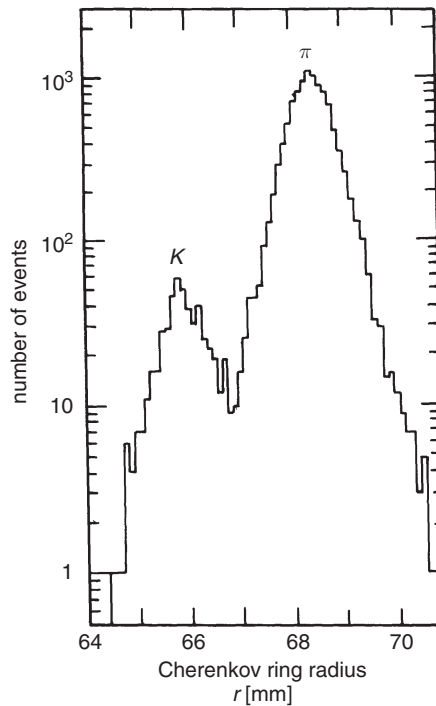


Fig. 9.8. Distribution of Cherenkov ring radii in a pion-kaon beam at 200 GeV/c. The Cherenkov photons have been detected in a multiwire proportional chamber filled with helium (83%), methane (14%) and TEA (3%). Calcium-fluoride crystals (CaF_2 crystal), having a high transparency in the ultraviolet region, were used for the entrance window [44].

compared to pions, and consequently produce, see Eqs. (9.14) and (9.15), Cherenkov rings with smaller radii [44].

Better *Cherenkov rings* are obtained from fast heavy ions, because the number of produced photons is proportional to the square of the projectile charge. Figure 9.9 [45] shows an early measurement of a Cherenkov ring produced by a relativistic heavy ion. The centre of the ring is also visible since the ionisation loss in the photon detector leads to a high energy deposit at the centre of the ring (see Fig. 9.7). Spurious signals, normally not lying on the Cherenkov ring, are caused by δ rays, which are produced in interactions of heavy ions with the chamber gas.

Figure 9.10 [46] shows an example of Cherenkov rings obtained by superimposing 100 collinear events from a monoenergetic collinear particle beam. The four square contours show the size of the calcium-fluoride



Fig. 9.9. Cherenkov ring of a relativistic heavy ion in a RICH counter [45].

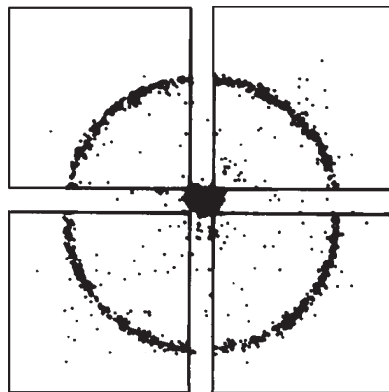


Fig. 9.10. Superposition of Cherenkov rings of 100 collinear events in a RICH counter. The square contours indicate the calcium-fluoride entrance windows of the photon detector [46].

crystals ($10 \times 10 \text{ cm}^2$ each), which served as the entrance window for the photon detector. The ionisation loss of the particles is also seen at the centre of the Cherenkov rings.

At present TEA and TMAE are still used widely as photo-converters, but solid CsI photocathodes become popular in RICH detectors. In addition to the gaseous or crystal radiators recently aerogel came in use as a Cherenkov medium. In modern RICH projects single- and multi-anode conventional PM tubes as well as hybrid PM tubes are often used (see reviews [25, 43, 47, 48] and references therein). Micropattern gaseous detectors (see Sect. 7.4) with a CsI photocathode are also good candidates as photon sensors for RICH systems. Modern RICH detectors are characterised by a number of photoelectrons in the range of 10–30 per ring and a resolution on the Cherenkov angle of $\sigma_{\theta_c} \approx 3\text{--}5 \text{ mrad}$ [40, 49]. Figure 9.11 (left) exhibits two intersecting Cherenkov rings measured by a system of multichannel PMTs in the HERA-B RICH detector [50]. The right part of this figure shows the reconstructed Cherenkov angle in its dependence on the particle momentum. A resolution of $\sigma_{\theta_c} \approx 1 \text{ mrad}$ for momenta exceeding 10 GeV is achieved.

It is even possible to obtain Cherenkov rings from electromagnetic cascades initiated by high-energy electrons or photons. The secondary particles produced during cascade development in the radiator follow closely the direction of the incident particle. They are altogether highly relativistic and therefore produce concentric rings of Cherenkov light with

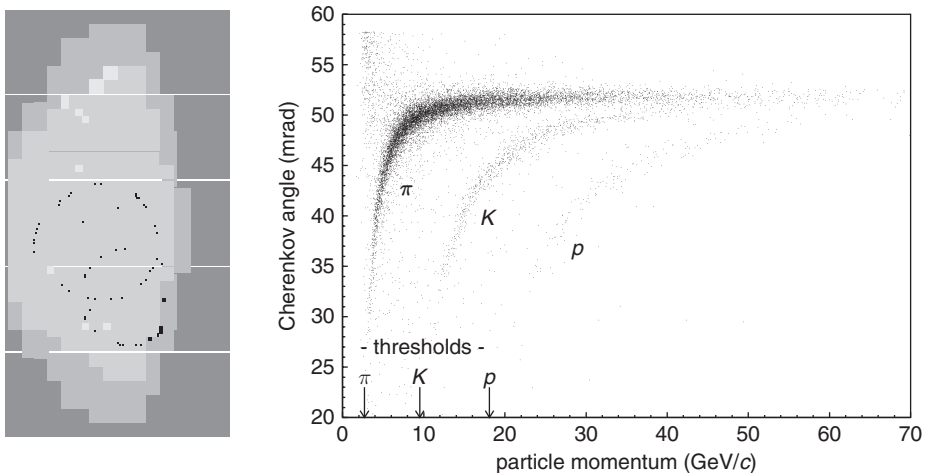


Fig. 9.11. Left: two intersecting Cherenkov rings measured by the system of multichannel PMTs in the HERA-B RICH detector. Right: reconstructed Cherenkov angle in the same detector [50].

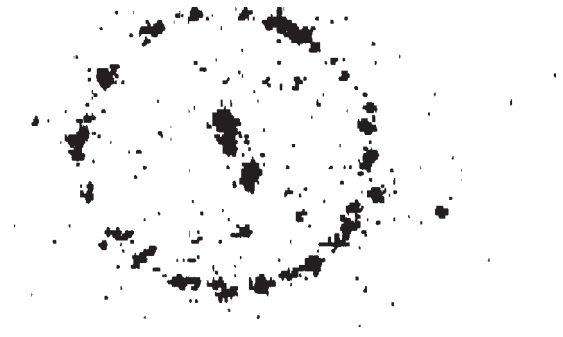


Fig. 9.12. Cherenkov ring produced by a high-energy (5 GeV) electron [51].

equal radii lying on top of one another. Figure 9.12 shows a distinct Cherenkov ring produced by a 5 GeV electron [51]. The large number of produced Cherenkov photons can be detected via the photoelectric effect in a position-sensitive detector.

The shape and position of such Cherenkov rings (elliptically distorted for inclined angles of incidence) can be used to determine the direction of incidence of high-energy gamma rays in the field of gamma-ray astronomy [52], where high-energy photons from cosmic-ray sources induce electromagnetic cascades in the Earth's atmosphere. Another example of particle identification by Cherenkov rings comes from neutrino physics. An important aspect of atmospheric neutrino studies is the correct identification of neutrino-induced muons and electrons. Figures 9.13 and 9.14 show a neutrino-induced event ($\nu_\mu + N \rightarrow \mu^- + X$) with subsequent (0.9 μs later) decay $\mu^- \rightarrow e^- + \bar{\nu}_e + \nu_\mu$ in the SNO experiment which contains a spherical vessel with 1000 tons of heavy water viewed by 10 000 PMTs [53]. The particle-identification capability of large-volume neutrino detectors is clearly seen.

A new generation of Cherenkov detectors uses the internal reflection in the radiator along with a PM-tube readout of the photons. The idea of the DIRC (Detector of Internally Reflected Cherenkov light), which was developed for particle identification in the BaBar detector [54], is illustrated in Fig. 9.15. The radiators of this detector are quartz bars of rectangular cross section. Most of the Cherenkov light generated by the particle is captured inside the bar due to internal reflection. The photon angle does not change during its travel with multiple reflections to the edge of the bar. After leaving the bar the photon is detected by PM tubes placed at some distance from the bar edge. Of course, quartz bars for this system should have the highest possible surface quality as well as a high accuracy of fabrication. The photon arrival time is measured as well – that helps to reject background hits.

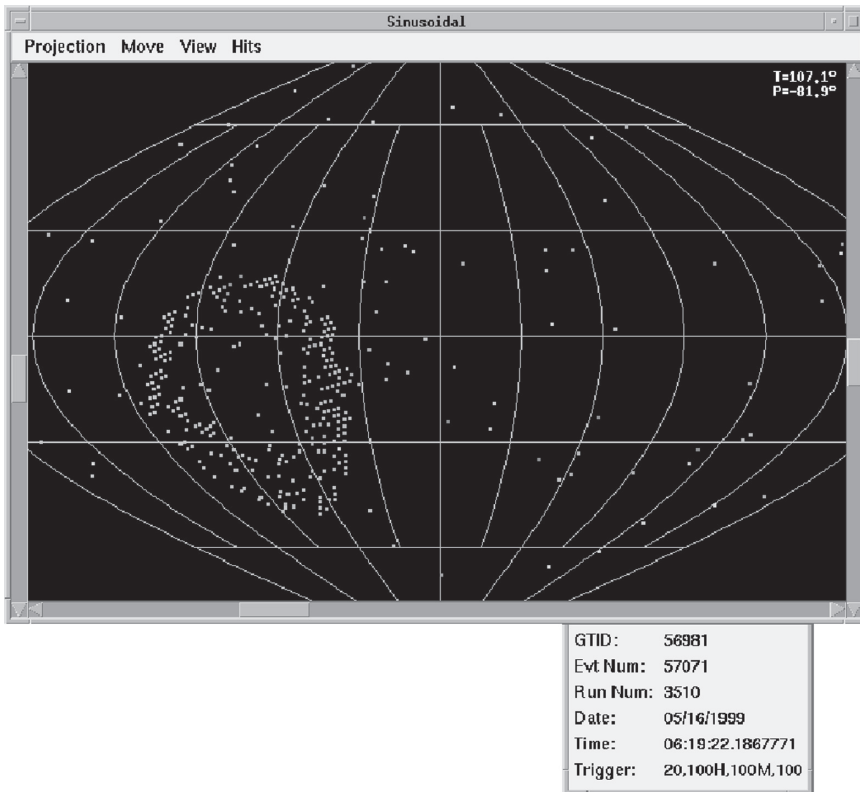


Fig. 9.13. Neutrino-induced muon in the SNO experiment [53].

The DIRC system of the BaBar detector contains 144 quartz bars that are 17 mm thick, 35 mm wide and 4.9 m long, which are viewed by the 896 PM tubes. The number of detected Cherenkov photons varies from 20 to 50 depending on the track's polar angle. This allows a reliable pion/kaon separation from 1 GeV to 4 GeV as shown in Fig. 9.16 [54, 55].

As discussed above, the basic DIRC idea is to measure two coordinates of the photons leaving the quartz bar, one of which is given by the end face of the quartz bar and the other by the impact position of the photon on the photon detector. However, to determine the Cherenkov angle, also two different variables, one spatial coordinate and the photon's time of propagation, are sufficient since one knows the particle track position and direction from the tracking system. This is the main idea of further developments of the Cherenkov-ring technique called the time-of-propagation (TOP) counter [56]. This device is quite promising and much more compact than a DIRC, however, it requires ultimate time resolution for single photons, better than 50 ps.

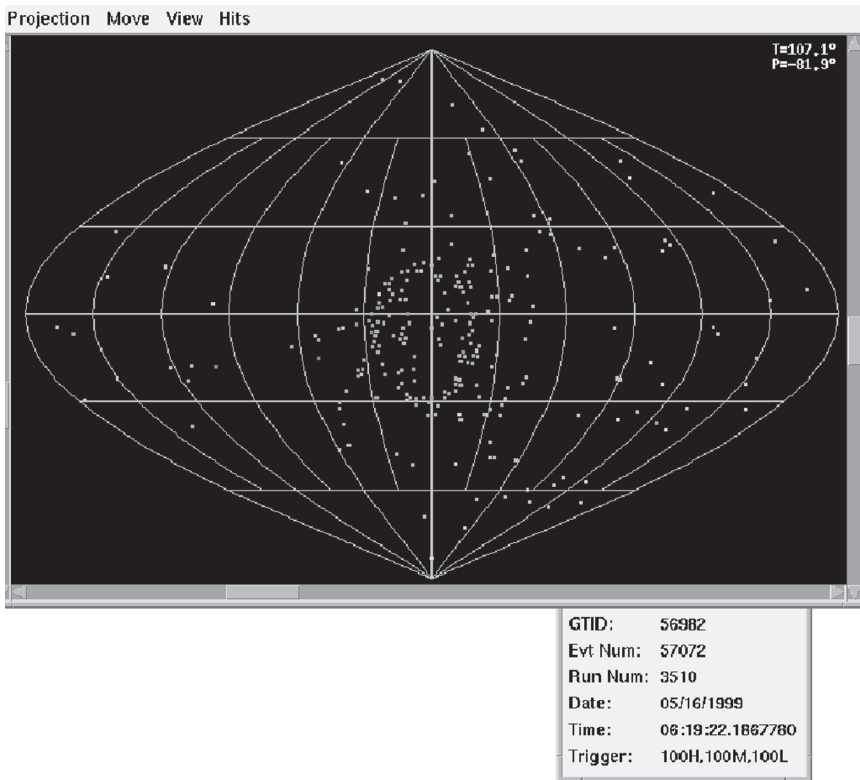


Fig. 9.14. Cherenkov ring produced by an electron from muon decay, where the muon was created by a muon neutrino [53].

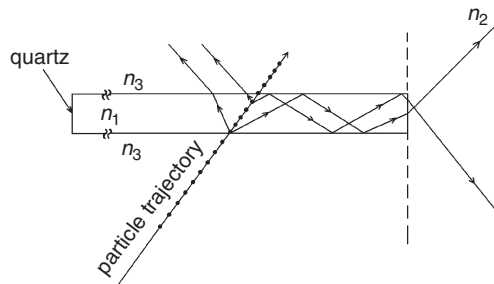


Fig. 9.15. The working principle of the DIRC counter [54].

9.1.4 Transition-radiation detectors

The effect of *transition radiation* [57] is used for high-energy particle identification in many current and planned experiments [58–62].

Let us consider as an example the ATLAS transition-radiation tracker (TRT). This sophisticated system is the largest present-day TRD detector

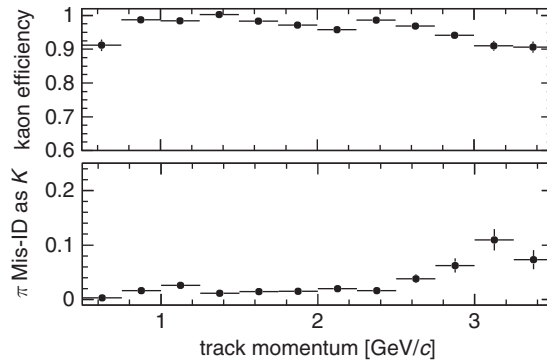


Fig. 9.16. Efficiency (top) and misidentification probability for pion/kaon separation (bottom) [55].

[62]. The TRT is part of the ATLAS inner detector and it is used both for charged-particle tracking and electron/pion separation. It consists of 370 000 cylindrical drift tubes (straws). Made from kapton and covered by a conductive film, the straw tube serves as cathode of a cylindrical proportional drift counter. A central 30 μm -diameter gold-plated tungsten wire serves as anode. The layers of straws are interleaved with polypropylene foils or fibres working as radiator. The tubes are filled with a gas mixture

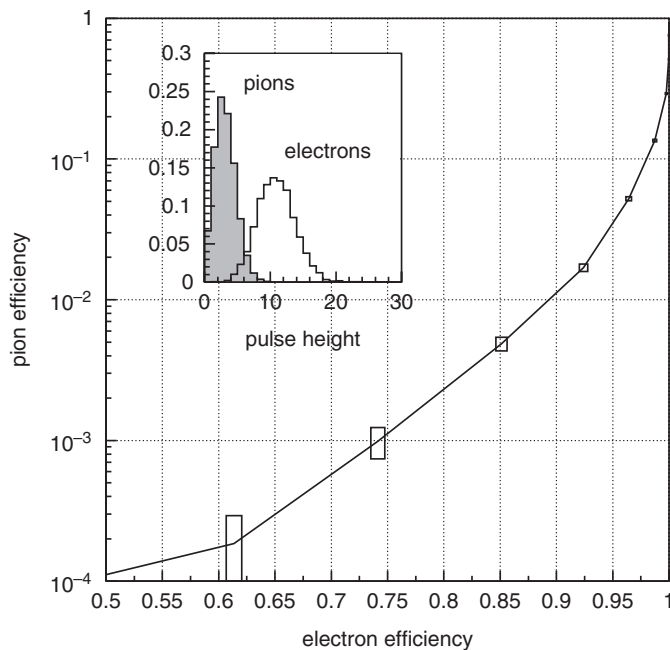


Fig. 9.17. Electron/pion separation capability measured with a prototype. The insert shows the energy depositions in a single straw for pions and electrons [63].

70% Xe + 27% CO₂ + 3% O₂, which provides a high X-ray absorption and proper counting characteristics.

The coordinate determination is performed by a drift-time measurement resulting in a spatial resolution of about 130 μm. The electron/pion separation is based on the energy deposition. A typical energy of the transition-radiation photon in the TRT is 8–10 keV, while a minimum-ionising particle deposits in one straw about 2 keV on average (see Fig. 9.17, left). As separation parameter the number of straws along the particle track having an energy deposition exceeding a certain threshold can be defined. Figure 9.18 shows a simulated event with a decay

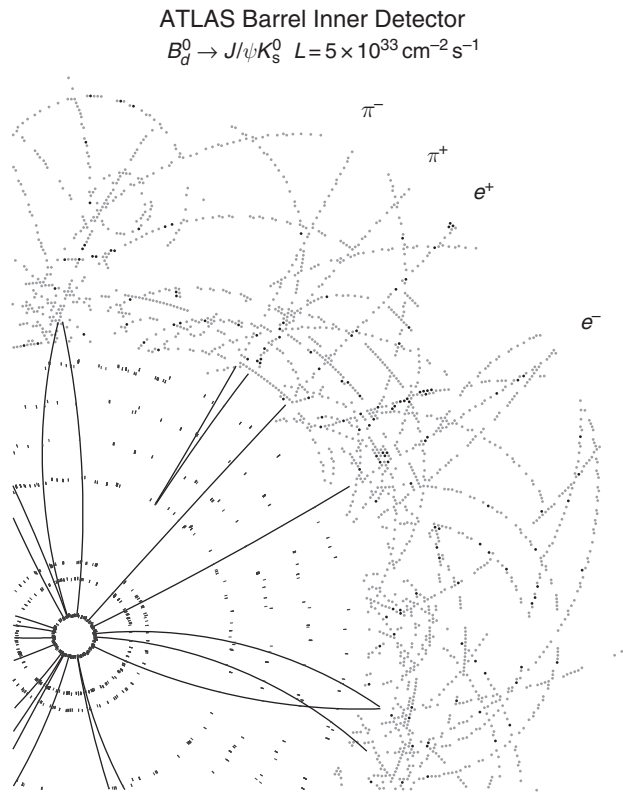


Fig. 9.18. A simulated event with a decay $B_d^0 \rightarrow J/\psi K_s$, where $J/\psi \rightarrow e^+e^-$ and $K_s \rightarrow \pi^+\pi^-$. Solid lines are reconstructed tracks beyond the TRT. Pion tracks are characterised by low energy depositions while electron tracks exhibit many straws with high energy deposition (black points > 6 keV, transition-radiation hits) [62]. It is also visible that low-energy δ electrons produced in ionisation processes with large energy transfers create high energy deposits because of the $1/\beta^2$ dependence of the ionisation energy loss. These unwanted ‘transition-radiation hits’ will complicate the pattern and particle identification.

$B_d^0 \rightarrow J/\psi K_s$, where $J/\psi \rightarrow e^+e^-$ and $K_s \rightarrow \pi^+\pi^-$. It is observed that the number of high-energy hits along electron tracks is larger than for pion tracks. The separation efficiency measured with a prototype straw chamber is presented in Fig. 9.17. For 90% electron efficiency, the probability of pion misidentification as electrons was measured to be 1.2% [63, 64].

TRD detectors are used rather widely for cosmic-ray experiments especially for the measurements above the Earth's atmosphere. For these experiments devices with a large sensitive area and low weight are required which are well met by TRDs [65]. Examples of such TRDs used or planned in the experiments HEAT, PAMELA and AMS can be found in [66–68]. It should be noted that the number of transition-radiation photons increases with z^2 of the particle, which makes it useful for the detection and identification of very high-energy ions. This TRD feature is used in astroparticle experiments as well; see, for example [69, 70], where it is of relevance for the determination of the chemical composition of high-energy cosmic rays.

9.2 Particle identification with calorimeters

In addition to energy determination, calorimeters are also capable of separating electrons from hadrons. The longitudinal and lateral shower development of electromagnetic cascades is determined by the radiation length X_0 , and that of hadronic cascades by the much larger nuclear interaction length λ_I . Calorimetric electron/hadron separation is based on these characteristic differences of shower development.

In contrast to TOF, dE/dx , Cherenkov or transition-radiation techniques, *calorimetric particle identification* is destructive in the sense that no further measurements can be made on the particles. Most particles end their journey in calorimeters. Muons and neutrinos are an exception.

Figure 9.19 [71] shows the longitudinal development of 100 GeV electron and pion showers in a streamer-tube calorimeter. Essentially, the separation methods are based on the difference in the longitudinal and lateral distributions of the energy deposition.

- Since for all materials normally used in calorimeters the nuclear interaction length λ_I is much larger than the radiation length X_0 , electrons interact earlier in the calorimeter compared to hadrons. Thus, electrons deposit the largest fraction of their energy in the front part of a calorimeter. Usually, the electromagnetic and hadron calorimeters are separated and the ratio of the energy deposited in the electromagnetic calorimeter to the particle momentum serves as an electron/hadron separation parameter. In case of a longitudinal segmentation of the

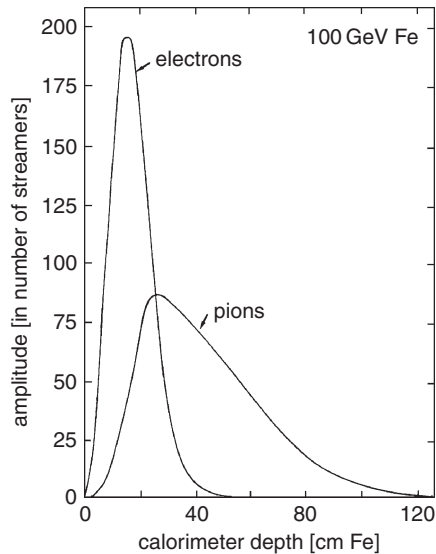


Fig. 9.19. Comparison of the longitudinal development of 100 GeV pions and electrons in a streamer-tube calorimeter [71].

calorimeter, the starting point of the shower development can be used as an additional separation criterion.

- Hadronic cascades are much wider compared to electromagnetic showers (see Figs. 8.6 and 8.19). In a compact iron calorimeter 95% of the electromagnetic energy is contained in a cylinder of 3.5 cm radius. For hadronic cascades the 95%-lateral-containment radius is larger by a factor of about five, depending on the energy. From the different lateral behaviour of electromagnetic and hadronic cascades a typical characteristic compactness parameter can be derived.
- Finally, the longitudinal centre of gravity of the shower can also be used as an electron/hadron separation criterion.

Each separation parameter can be used to define a likelihood function corresponding to the electron or pion hypothesis in an unseparated electron–pion beam. The combined likelihood function including functions for all separation parameters allows to obtain much better electron/pion separation in calorimeters. One must take into account, however, that the separation criteria may be strongly correlated. Figure 9.20 [72, 73] shows such combined parameter distributions exhibiting only a small overlap between the electron and pion hypothesis. The resulting e/π *misidentification* probability for a given electron efficiency is shown in Fig. 9.21 [72, 73]. For a 95% electron acceptance one obtains in this example a 1% pion contamination for a particle energy of 75 GeV. With more sophisticated

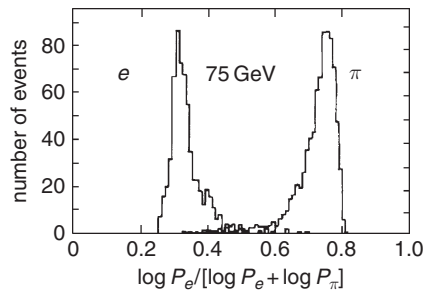


Fig. 9.20. Electron/pion separation in a streamer-tube calorimeter [72, 73].

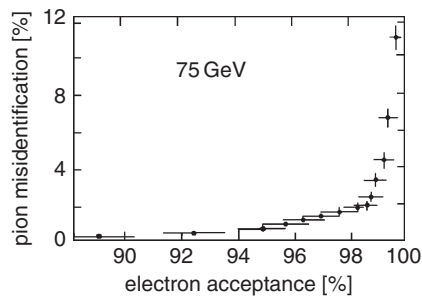


Fig. 9.21. Electron/pion misidentification probability in a streamer-tube calorimeter [72, 73]. The electron acceptance is the fraction of electrons accepted by a cut in the probability distribution. Correspondingly, the pion misidentification represents the fraction of accepted electron candidates that are really pions.

calorimeters a pion contamination as low as 0.1% can be reached with calorimetric methods.

Figure 9.22 demonstrates the separation capability of a crystal calorimeter for low-energy particles. The data were taken with the CMD-2 detector, in which the processes $e^+e^- \rightarrow e^+e^-$, $\mu^+\mu^-$, $\pi^+\pi^-$ were studied at a centre-of-mass energy of about 0.8 GeV. The two-dimensional plot presents the energy for final-state particles measured in the CsI-crystal electromagnetic calorimeter [74]. e^+e^- events concentrate in the upper right-hand corner while minimum-ionising particles, $\mu^+\mu^-$, $\pi^+\pi^-$, and a small admixture of the cosmic-ray background populate the lower left-hand area. The $\pi^+\pi^-$ distribution has long tails to higher energies due to pion nuclear interactions. The electrons are well separated from other particles. One can note that the event-separation quality strongly improves when one has two particles of the same type.

High-energy muons can be distinguished not only from pions but also from electrons by their low energy deposition in calorimeters and by their longer range. Figure 9.23 [71] shows the amplitude distributions of 50 GeV

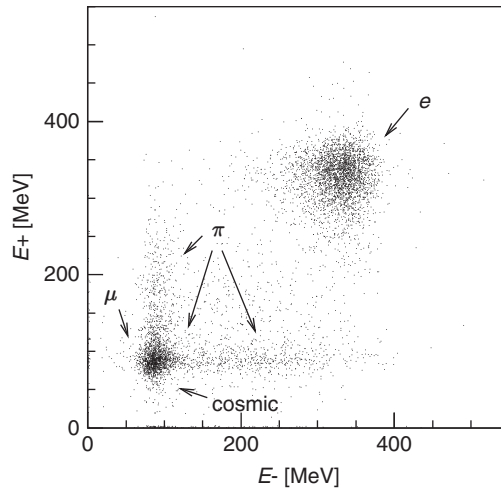


Fig. 9.22. The energies of final particles in $e^+e^- \rightarrow e^+e^-, \mu^+\mu^-, \pi^+\pi^-$ processes, measured by the CsI-crystal calorimeter of the CMD-2 detector [74]. The centre-of-mass energy of the experiment is about 0.8 GeV.

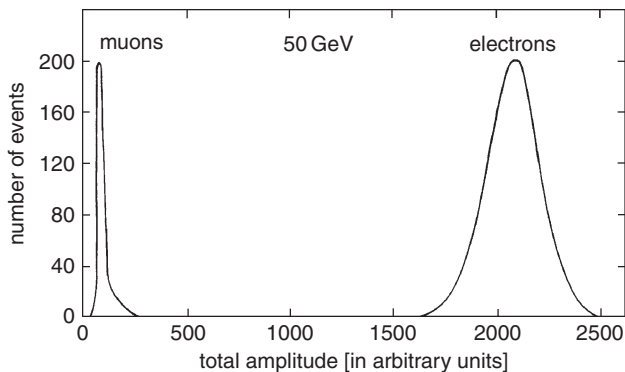


Fig. 9.23. Amplitude distribution of 50 GeV electrons and muons in a streamer-tube calorimeter [71].

electrons and muons. The possibility of an excellent electron/muon separation is already evident from this diagram.

The digital hit pattern of a 10 GeV pion, muon and electron in a streamer-tube calorimeter is shown in Fig. 9.24 [75]. Detectors operating at energies below 10–20 GeV are often equipped with a muon-range system instead of a hadron calorimeter. This system usually consists of absorber plates alternating with sensitive layers (see, e.g., Chap. 13). Then the particle of known momentum is identified by comparing the measured

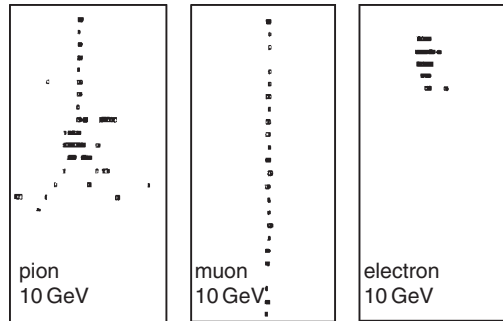


Fig. 9.24. Digital hit patterns (i.e. dot = fired tube) of 10 GeV pions, muons and electrons in a streamer-tube hadron calorimeter [75].

range with the one expected for a muon as well as by the lateral hit pattern.

For higher beam energies the interaction probability of muons for processes with higher energy transfers, e.g. by *muon bremsstrahlung*, increases [76–81]. Although these processes are still quite rare, they can nevertheless lead to a small μ/e misidentification probability in purely calorimetric measurements.

Since the energy loss of high-energy muons (> 500 GeV) in matter is dominated by processes with large energy transfers (bremsstrahlung, direct electron-pair production, nuclear interactions), and these energy losses are proportional to the muon energy, see Eq. (1.74), one can even build muon calorimeters for high energies in which the measurement of the muon energy loss allows an energy determination. This possibility of muon calorimetry will certainly be applied in proton–proton collision experiments at the highest energies (LHC – Large Hadron Collider, $\sqrt{s} = 14$ TeV; ELOISATRON, $\sqrt{s} = 200$ TeV [82]). The calorimetric method of muon energy determination can also be employed in deep-water and ice experiments used as neutrino telescopes.

9.3 Neutron detection

Depending on the energy of the neutrons, different detection techniques must be employed. Common to all methods is that charged particles have to be produced in neutron interactions, which then are seen by the detector via ‘normal’ interaction processes like, e.g. ionisation or the production of light in scintillators [83–85].

For low-energy neutrons ($E_n^{\text{kin}} < 20 \text{ MeV}$) the following conversion reactions can be used:



The cross sections for these reactions depend strongly on the neutron energy. They are plotted in Fig. 9.25 [85].

For energies between $20 \text{ MeV} \leq E_n \leq 1 \text{ GeV}$ the production of recoil protons via the elastic (n,p) scattering can be used for neutron detection, Eq. (9.20). Neutrons of high energy ($E_n > 1 \text{ GeV}$) produce hadron cascades in inelastic interactions which are easy to identify.

To be able to distinguish neutrons from other particles, a *neutron counter* basically always consists of an anti-coincidence counter, which vetoes charged particles, and the actual neutron detector.

Thermal neutrons ($E_n \approx \frac{1}{40} \text{ eV}$) are easily detected with ionisation chambers or proportional counters, filled with boron-trifluoride gas (BF_3). To be able to detect higher-energy neutrons also in these counters, the neutrons first have to be moderated, since otherwise the neutron interaction cross section would be too small (see Fig. 9.25). The moderation of non-thermal neutrons can best be done with substances containing many protons, because neutrons can transfer a large amount of energy to collision partners of the same mass. In collisions with heavy nuclei essentially only elastic scattering with small energy transfers occurs. Paraffin or water are preferred moderators. Neutron counters for non-thermal neutrons are

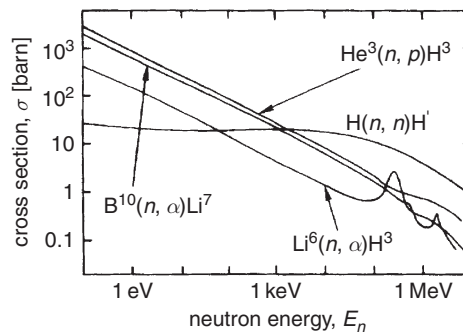


Fig. 9.25. Cross sections for neutron-induced reactions as a function of the neutron energy (1 barn = 10^{-24} cm^2) [85].

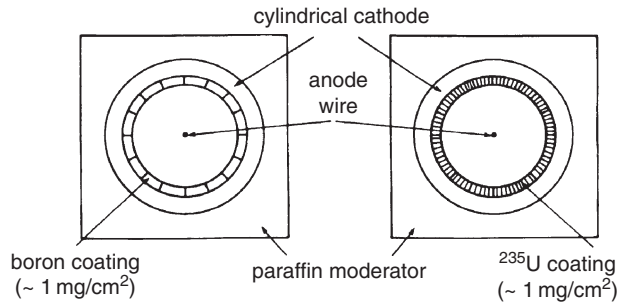


Fig. 9.26. Neutron detection with proportional counters [83].

therefore covered with these substances. With BF_3 counters, neutron detection efficiencies on the order of 1% can be achieved.

Thermal neutrons can also be detected via a fission reaction (n, f) ($f = \text{fission}$). Figure 9.26 shows two special proportional counters which are covered on the inside with either a thin boron or uranium coating to induce the neutrons to undergo either (n, α) or (n, f) reactions [83]. To moderate fast neutrons these counters are mounted inside a paraffin barrel.

Thermal or *quasi-thermal neutrons* can also be detected with solid-state detectors. For this purpose, a lithium-fluoride (^6LiF) coating is evaporated onto the surface of a semiconductor counter in which, according to Eq. (9.17), α particles and tritons are produced. These can easily be detected by the solid-state detector.

Equally well europium-doped lithium-iodide scintillation counters $\text{LiI}(\text{Eu})$ can be used for neutron detection since α particles and tritons produced according to Eq. (9.17) can be measured via their scintillation light. Slow neutrons or neutrons with energies in the MeV range can be detected in multiwire proportional chambers filled with a gas mixture of ^3He and Kr at high pressure by means of the Reaction (9.19).

For *slow neutrons*, due to momentum conservation, ^3H and p are produced back to back. From the reaction kinematics one can find $E_p = 0.57 \text{ MeV}$ and $E(^3\text{H}) = 0.19 \text{ MeV}$.

A typical neutron counter based on this reaction commonly employed in the field of radiation protection normally uses polyethylene spheres as moderator along with a ^3He -recoil proportional detector. Since the cross section for Reaction (9.19) is strongly energy-dependent, the performance and the sensitivity of such a counter can be improved by neutron absorbers in the moderator. Using special gas fillings – mainly $^3\text{He}/\text{CH}_4$ are used – the yield of recoil protons and tritons can be optimised. The moderator parameters can be determined by appropriate simulation programs for neutron transport [86].

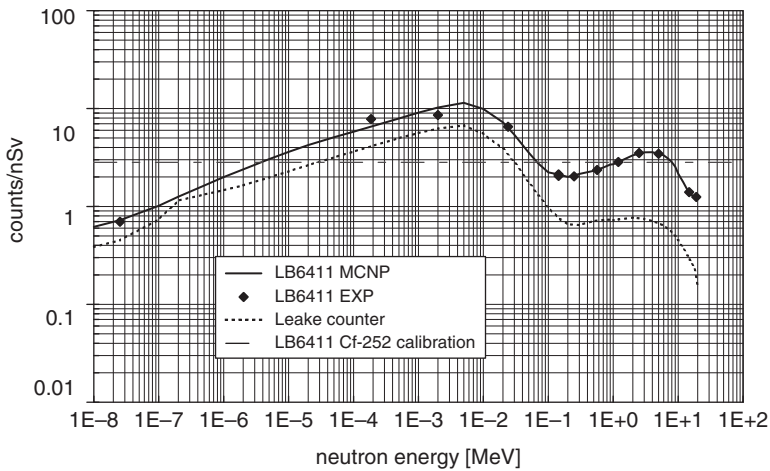


Fig. 9.27. Energy dependence of the neutron detection sensitivity of ^3He proportional counters with polyethylene shielding (from [87, 88]).

Typical sensitivities of several counts per nano-Sievert can be achieved with a scatter of $\pm 30\%$ for neutron energies between 50 keV and 10 MeV. For lower energies (10 meV to 100 eV) larger variations in sensitivity are unavoidable (Fig. 9.27, [87, 88]).

Due to the massive moderator the sensitivity for α , β or γ radiation is extremely small making such a ^3He counter ideally suited for reliable neutron measurements even in an environment of other radiation fields.

Possible applications are neutron dosimeters in nuclear power plants or hospitals where separate neutron-dose measurements are required because the *relative biological effectiveness* of neutrons is rather high compared to β and γ rays. It is also conceivable to search for illegal trafficking of radioactive neutron-emitting sources (such as weapon-grade plutonium) or for hidden sources which are otherwise difficult to detect, because α , β or γ rays can easily be shielded while neutrons cannot, providing a possibility to trace radioactive material [87, 88].

The elastic recoil reaction (9.20) can also be used in multiwire proportional chambers containing hydrogen-rich components (e.g. $\text{CH}_4 + \text{Ar}$). The size of a neutron counter should be large compared to the maximum range of the recoil protons: 10 cm in typical gases [89]. In solids the range of protons is reduced approximately in reverse proportion to the density (see Sect. 1.1.9).

Neutrons in the energy range 1–100 MeV can also be detected in organic scintillation counters via the production of recoil protons (i.e. via the $\text{H}(n, n')\text{H}'$ reaction) according to Eq. (9.20). However, the cross section

Table 9.1. *Threshold reactions for neutron energy measurements [83]*

Reaction	Threshold energy [MeV]
Fission of ^{234}U	0.3
Fission of ^{236}U	0.7
$^{31}\text{P} (n, p) ^{31}\text{Si}$	0.72
$^{32}\text{S} (n, p) ^{32}\text{P}$	0.95
Fission of ^{238}U	1.3
$^{27}\text{Al} (n, p) ^{27}\text{Mg}$	1.9
$^{56}\text{Fe} (n, p) ^{56}\text{Mn}$	3.0
$^{27}\text{Al} (n, \alpha) ^{24}\text{Na}$	3.3
$^{24}\text{Mg} (n, p) ^{24}\text{Na}$	4.9
$^{65}\text{Cu} (n, 2n) ^{64}\text{Cu}$	10.1
$^{58}\text{Ni} (n, 2n) ^{57}\text{Ni}$	12.0

for this reaction decreases rapidly with increasing neutron energy (see Fig. 9.25) so that the neutron-detection efficiency is reduced. For neutrons of 10 MeV the np scattering cross section is about 1 barn. Then, for an organic scintillator of 1 cm thickness (density $\rho = 1.2 \text{ g/cm}^3$ assumed) with a 30% molar fraction of free protons, a neutron-detection efficiency of about 2.5% is obtained.

In some applications – e.g. in the field of radiation protection – the measurement of the *neutron energy* is of great importance because the relative biological effectiveness of neutrons is strongly energy-dependent. The measurement of the neutron energy is frequently carried out with threshold detectors. Such a detector consists of a carrier foil covered with an isotope that only reacts with neutrons above a certain threshold energy. The particles or charged nuclei liberated in these reactions can be detected, e.g. in plastic detectors (cellulose-nitrate or cellulose-acetate foils) by an etching technique, and evaluated under a microscope or with automatic pattern-recognition methods (compare Sect. 6.11). Table 9.1 lists several threshold reactions used for neutron detection.

To cover different energy ranges of neutrons in a single exposure, one uses stacks of plastic foils coated with different isotopes. From the counting rates in the individual carrier foils with different energy thresholds, a rough determination of the neutron energy spectrum can be performed [83].

9.4 Problems

- 9.1** What are the Cherenkov angles for 3, 4 and 5 GeV/ c pions in Lucite, silica aerogel, Pyrex and lead glass?

	index of refraction
Lucite	1.49
silica aerogel	1.025–1.075
Pyrex	1.47
lead glass	1.92

- 9.2** Calculate the Cherenkov energy emitted in water in the visible range (400–700 nm) per cm by a 2.2 GeV/ c kaon!
- 9.3** How would you design a water Cherenkov detector that gives about 12 collected photoelectrons for 5 GeV/ c protons?
Assume that the quantum efficiency of the used photomultiplier is 20%, the light collection efficiency to be 25% and the transfer probability from the photocathode to the first dynode to be 80%.
- 9.4** A 3 GeV/ c proton is passing through Lucite. Estimate the number of visible photons emitted by δ rays using an approximation for dE/dx over the relevant energy range? Assume a radiator thickness of $x = 10 \text{ g/cm}^2$ ($\hat{=}$ 6.71 cm).
- 9.5** The Cherenkov angle of relativistic particles in air ($n = 1.000295$) is 1.4° . Still, in experiments with Imaging Air Cherenkov telescopes typical Cherenkov angles around 1° are reported. What is the reason for that?
- 9.6** In an experiment for particle identification the energy loss dE/dx is measured in a $300 \mu\text{m}$ silicon counter and the energy is obtained from a total-absorption calorimeter. In a mixed beam of muons and pions of 10 MeV kinetic energy a product $\Delta E \cdot E_{\text{kin}} = 5.7 \text{ MeV}^2$ is obtained. Was this due to a muon or a pion?

$$(\rho_{\text{Si}} = 2.33 \text{ g/cm}^3, Z_{\text{Si}} = 14, A_{\text{Si}} = 28, I_{\text{Si}} \approx 140 \text{ eV}.)$$

The same setup is used to separate the beryllium isotopes ${}^7\text{Be}$ and ${}^9\text{Be}$ of 100 MeV kinetic energy with the result $\Delta E \cdot E_{\text{kin}} = 3750 \text{ MeV}^2$. Identify the beryllium isotope that produced this result. Why did ${}^8\text{Be}$ not show up in this beam of beryllium isotopes?

$$(m({}^7\text{Be}) = 6.55 \text{ GeV}/c^2, m({}^9\text{Be}) = 8.42 \text{ GeV}/c^2.)$$

References

- [1] W. Klempt, Review of Particle Identification by Time of Flight Techniques, *Nucl. Instr. Meth.* **A433** (1999) 542–53
- [2] M. Bonesini, *A Review of Recent Techniques of TOF Detectors*, Proc. 8th Int. Conf. on Advanced Technology and Particle Physics (ICATPP 2003): Astroparticle, Particle, Space Physics, Detectors and Medical Physics Applications, Como, Italy, 6–10 October 2003, Como 2003, Astroparticle, Particles and Space Physics, Detectors and Medical Physics Applications, 455–61
- [3] Y. Kubota *et al.*, The CLEO II Detector, *Nucl. Instr. Meth.* **A320** (1992) 66–113
- [4] H. Kichimi *et al.*, The BELLE TOF System, *Nucl. Instr. Meth.* **A453** (2000) 315–20
- [5] Ch. Paus *et al.*, Design and Performance Tests of the CDF Time-of-Flight System, *Nucl. Instr. Meth.* **A461** (2001) 579–81; S. Cabrera *et al.*, The CDF Time of Flight Detector, FERMILAB-CONF-03-404-E (2004)
- [6] G. Osteria *et al.*, The Time-of-Flight System of the PAMELA Experiment on Satellite, *Nucl. Instr. Meth.* **A535** (2004) 152–7
- [7] S. Denisov *et al.*, Characteristics of the TOF Counters for GlueX Experiment, *Nucl. Instr. Meth.* **A494** (2002) 495–9
- [8] M. Akatsu *et al.*, MCP-PMT Timing Property for Single Photons, *Nucl. Instr. Meth.* **A528** (2004) 763–75
- [9] Y. Enari *et al.*, Cross-talk of a Multi-anode PMT and Attainment of a sigma Approx. 10-ps TOF Counter, *Nucl. Instr. Meth.* **A547** (2005) 490–503
- [10] K. Inami *et al.*, A 5 ps TOF-Counter with an MCP-PMT, *Nucl. Instr. Meth.* **A560** (2006) 303–8
- [11] K. Kleinknecht, *Detektoren für Teilchenstrahlung*, Teubner, Stuttgart (1984, 1987, 1992); *Detectors for Particle Radiation*, Cambridge University Press, Cambridge (1986)
- [12] W. Braunschweig, Spark Gaps and Secondary Emission Counters for Time of Flight Measurement, *Phys. Scripta* **23** (1981) 384–92
- [13] M.V. Babykin *et al.*, Plane-Parallel Spark Counters for the Measurement of Small Times; Resolving Time of Spark Counters, *Sov. J. Atomic Energy* **IV** (1956) 627–34; Atomic Energy, Engineering, Physics and Astronomy and Russian Library of Science, Springer, **1(4)** (1956) 487–94
- [14] V.V. Parkhomchuck, Yu.N. Pestov & N.V. Petrovykh, A Spark Counter with Large Area, *Nucl. Instr. Meth.* **A93** (1971) 269–70
- [15] E. Badura *et al.*, Status of the Pestov Spark Counter Development for the ALICE Experiment, *Nucl. Instr. Meth.* **A379** (1996) 468–71
- [16] I. Crotty *et al.*, Investigation of Resistive Plate Chambers, *Nucl. Instr. Meth.* **A329** (1993) 133–9
- [17] E. Cerron-Zeballos *et al.*, A Very Large Multigap Resistive Plate Chamber, *Nucl. Instr. Meth.* **A434** (1999) 362–72

- [18] A. Peisert, G. Charpak, F. Sauli & G. Viezzoli, Development of a Multistep Parallel Plate Chamber as Time Projection Chamber Endcap or Vertex Detector, *IEEE Trans. Nucl. Sci.* **31** (1984) 125–9
- [19] P. Astier *et al.*, Development and Applications of the Imaging Chamber, *IEEE Trans. Nucl. Sci.* **NS-36** (1989) 300–4
- [20] V. Peskov *et al.*, Organometallic Photocathodes for Parallel-Plate and Wire Chambers, *Nucl. Instr. Meth.* **A283** (1989) 786–91
- [21] M. Izycki *et al.*, *A Large Multistep Avalanche Chamber: Description and Performance*, in Proc. 2nd Conf. on Position Sensitive Detectors, London (4–7 September 1990), *Nucl. Instr. Meth.* **A310** (1991) 98–102
- [22] G. Charpak *et al.*, *Investigation of Operation of a Parallel Plate Avalanche Chamber with a CsI Photocathode Under High Gain Conditions*, CERN-PPE-91-47 (1991); *Nucl. Instr. Meth.* **A307** (1991) 63–8
- [23] Yu.N. Pestov, Review on Counters with Localised Discharge, *Nucl. Instr. Meth.* **A494** (2002) 447–54
- [24] J.N. Marx & D.R. Nygren, The Time Projection Chamber, *Physics Today* (October 1978) 46–53
- [25] J. Va'vra, Particle Identification Methods in High-Energy Physics, *Nucl. Instr. Meth.* **A453** (2000) 262–78
- [26] M. Hauschild, Progress in dE/dx Techniques Used for Particle Identification, *Nucl. Instr. Meth.* **A379** (1996) 436–41
- [27] K. Affholderbach *et al.*, Performance of the New Small Angle Monitor for Background (SAMBA) in the ALEPH Experiment at CERN, *Nucl. Instr. Meth.* **A410** (1998) 166–75
- [28] I. Lehraus *et al.*, Performance of a Large Scale Multilayer Ionization Detector and its Use for Measurements of the Relativistic Rise in the Momentum Range of 20–110 GeV/c, *Nucl. Instr. Meth.* **153** (1978) 347–55
- [29] W.T. Eadie *et al.*, *Statistical Methods in Experimental Physics*, Elsevier–North Holland, Amsterdam/London (1971)
- [30] W.B. Atwood *et al.*, Performance of the ALEPH Time Projection Chamber, *Nucl. Instr. Meth.* **A306** (1991) 446–58
- [31] A. Ngac, Diploma Thesis, University of Siegen, 2000
- [32] J.M. Link *et al.*, Cherenkov Particle Identification in FOCUS, *Nucl. Instr. Meth.* **A484** (2002) 270–86
- [33] A.Yu. Barnyakov *et al.*, Development of Aerogel Cherenkov Detectors at Novosibirsk, *Nucl. Instr. Meth.* **A553** (2005) 125–9
- [34] B. Tonguc *et al.*, The BLAST Cherenkov Detectors, *Nucl. Instr. Meth.* **A553** (2005) 364–9
- [35] E. Cuautle *et al.*, Aerogel Cherenkov Counters for High Momentum Proton Identification, *Nucl. Instr. Meth.* **A553** (2005) 25–9
- [36] J. Seguinot & T. Ypsilantis, Photo-Ionization and Cherenkov Ring Imaging, *Nucl. Instr. Meth.* **142** (1977) 377–91
- [37] E. Nappi & T. Ypsilantis (eds.), *Experimental Techniques of Cherenkov Light Imaging*, Proc. of the First Workshop on Ring Imaging Cherenkov Detectors, Bari, Italy 1993; *Nucl. Instr. Meth.* **A343** (1994) 1–326
- [38] C.W. Fabjan & H.G. Fischer, *Particle Detectors*, CERN-EP-80-27 (1980)

- [39] K. Abe *et al.*, Operational Experience with SLD CRID at the SLC, *Nucl. Instr. Meth.* **A379** (1996) 442–3
- [40] M. Artuso *et al.*, Construction, Pattern Recognition and Performance of the CLEO III LiF-TEA RICH Detector, *Nucl. Instr. Meth.* **A502** (2003) 91–100
- [41] C. Matteuzzi, Particle Identification in LHCb, *Nucl. Instr. Meth.* **A494** (2002) 409–15
- [42] H.E. Jackson, The HERMES Dual-Radiator RICH Detector, *Nucl. Instr. Meth.* **A502** (2003) 36–40
- [43] J. Va'vra, *Cherenkov Imaging Techniques for the Future High Luminosity Machines*, SLAC-Pub-11019 (September 2003)
- [44] T. Ekelöf, *The Use and Development of Ring Imaging Cherenkov Counters*, CERN-PPE-91-23 (1991)
- [45] R. Stock, NA35-Collaboration, private communication (1990)
- [46] F. Sauli, *Gas Detectors: Recent Developments and Applications*, CERN-EP-89-74 (1989); and Le Camere Proporzionali Multifili: Un Potente Instrumento Per la Ricerca Applicata, *Il Nuovo Saggiatore* **2** (1986) 2/26
- [47] J. Seguinot & T. Ypsilantis, Evolution of the RICH Technique, *Nucl. Instr. Meth.* **A433** (1999) 1–16
- [48] F. Piuz, Ring Imaging Cherenkov Systems Based on Gaseous Photo-Detectors: Trends and Limits around Particle Accelerators, *Nucl. Instr. Meth.* **A502** (2003) 76–90
- [49] F. Piuz *et al.*, Final Tests of the CsI-based Ring Imaging Detector for the ALICE Experiment, *Nucl. Instr. Meth.* **A433** (1999) 178–89
- [50] I. Arino *et al.*, The HERA-B Ring Imaging Cherenkov Counter, *Nucl. Instr. Meth.* **A516** (2004) 445–61
- [51] *Cherenkov Telescopes for Gamma-Rays*, CERN-Courier **28(10)** (1988) 18–20
- [52] E. Lorenz, Air Shower Cherenkov Detectors, *Nucl. Instr. Meth.* **A433** (1999) 24–33
- [53] Sudbury Neutrino Observatory home page: www.sno.phy.queensu.ca/sno/events/
- [54] I. Adam *et al.*, The DIRC Particle Identification System for the BABAR Experiment, *Nucl. Instr. Meth.* **A538** (2005) 281–357
- [55] J. Schwiening, The DIRC Detector at the SLAC B-factory PEP-II: Operational Experience and Performance for Physics Applications, *Nucl. Instr. Meth.* **A502** (2003) 67–75
- [56] Y. Enari *et al.*, Progress Report on Time-of-Propagation Counter – A New Type of Ring Imaging Cherenkov Detector, *Nucl. Instr. Meth.* **A494** (2002) 430–5
- [57] V.L. Ginzburg & I.M. Frank, Radiation of a Uniformly Moving Electron due to its Transitions from One Medium into Another, *JETP* **16** (1946) 15–29
- [58] G. Bassompierre *et al.*, A Large Area Transition Radiation Detector for the NOMAD Experiment, *Nucl. Instr. Meth.* **A403** (1998) 363–82
- [59] K.N. Barish *et al.*, TEC/TRD for the PHENIX Experiment, *Nucl. Instr. Meth.* **A522** (2004) 56–61

- [60] www-alice.gsi.de/trd/
- [61] J.D. Jackson, *Classical Electrodynamics*, 3rd edition, John Wiley & Sons, New York (1998); L.C.L. Yuan & C.S. Wu (eds.), *Methods of Experimental Physics*, Vol. 5A, Academic Press, New York (1961) 163; W.W.M. Allison & P.R.S. Wright, The Physics of Charged Particle Identification: dE/dx, Cherenkov Radiation and Transition Radiation, in T. Ferbel (ed.), *Experimental Techniques in High Energy Physics*, Addison-Wesley, Menlo Park, CA (1987) 371
- [62] ATLAS Inner Detector Community, Inner detector. Technical design report, Vol. II, ATLAS TDR 5, CERN/LHCC 97-17 (1997); Fido Dittus, private communication (2006)
- [63] V.A. Mitsou for the ATLAS collaboration, *The ATLAS Transition Radiation Tracker*, Proc. of 8th Int. Conf. on Advanced Technology and Particle Physics (ICATPP 2003), Astroparticle, Particle, Space Physics, Detectors and Medical Physics Applications, Como, Italy (6–10 October 2003) 497–501
- [64] T. Akesson *et al.*, ATLAS Transition Radiation Tracker Test-Beam Results, *Nucl. Instr. Meth.* **A522** (2004) 50–5
- [65] D. Müller, Transition Radiation Detectors in Particle Astrophysics, *Nucl. Instr. Meth.* **A522** (2004) 9–15
- [66] S.W. Barwick *et al.*, The High-Energy Antimatter Telescope (HEAT): An Instrument for the Study of Cosmic-Ray Positrons, *Nucl. Instr. Meth.* **A400** (2004) 34–52
- [67] M. Ambriola and PAMELA Collaboration, Performance of the Transition Radiation Detector of the PAMELA Space Mission, *Nucl. Phys. B Proc. Suppl.* **113** (2002) 322–8
- [68] F.R. Spada, The AMS Transition Radiation Detector, *Int. J. Mod. Phys.* **A20** (2005) 6742–4
- [69] J. L’Heureux *et al.*, A Detector for Cosmic-Ray Nuclei at Very High Energies, *Nucl. Instr. Meth.* **A295** (1990) 246–60
- [70] F. Gahbauer *et al.*, A New Measurement of the Intensities of the Heavy Primary Cosmic-Ray Nuclei around 1 TeV amu, *Astrophys. J.* **607** (2004) 333–41
- [71] R. Baumgart, *Messung und Modellierung von Elektron- und Hadron-Kaskaden in Streamerrohrkalorimetern*, Ph.D. Thesis, University of Siegen (1987)
- [72] U. Schäfer, *Untersuchungen zur Magnetfeldabhängigkeit und Pion/Elektron Unterscheidung in Elektron-Hadron Kalorimetern*, Ph.D. Thesis, University of Siegen (1987)
- [73] R. Baumgart *et al.*, Electron–Pion Discrimination in an Iron/Streamer Tube Calorimeter up to 100 GeV, *Nucl. Instr. Meth.* **272** (1988) 722–6
- [74] R.R. Akhmetshin *et al.*, Measurement of $e^+e^- \rightarrow \pi^+\pi^-$ Cross-section with CMD-2 around ρ -meson, *Phys. Lett.* **B527** (2002) 161–72
- [75] ALEPH Collaboration, D. Decamp *et al.*, ALEPH: A Detector for Electron–Positron Annihilations at LEP, *Nucl. Instr. Meth.* **A294** (1990) 121–78
- [76] C. Grupen, Electromagnetic Interactions of High Energy Cosmic Ray Muons, *Fortschr. der Physik* **23** (1976) 127–209

- [77] W. Lohmann, R. Kopp & R. Voss, *Energy Loss of Muons in the Energy Range 1 – 10.000 GeV*, CERN-85-03 (1985)
- [78] W.K. Sakumoto *et al.*, *Measurement of TeV Muon Energy Loss in Iron*, University of Rochester UR-1209 (1991); *Phys. Rev.* **D45** (1992) 3042–50
- [79] R. Baumgart *et al.*, Interaction of 200 GeV Muons in an Electromagnetic Streamer Tube Calorimeter, *Nucl. Instr. Meth.* **A258** (1987) 51–7
- [80] C. Zupancic, *Physical and Statistical Foundations of TeV Muon Spectroscopy*, CERN-EP-85-144 (1985)
- [81] M.J. Tannenbaum, *Comparison of Two Formulas for Muon Bremsstrahlung*, CERN-PPE-91-134 (1991)
- [82] E. Nappi & J. Seguinot (eds.), *INFN Eloisatron Project: 42nd Workshop On Innovative Detectors For Supercolliders*, World Scientific, Singapore (2004)
- [83] E. Sauter, *Grundlagen des Strahlenschutzes*, Siemens AG, Berlin/München (1971); *Grundlagen des Strahlenschutzes*, Thiemig, München (1982)
- [84] W. Schneider, *Neutronenmeßtechnik*, Walter de Gruyter, Berlin/ New York (1973)
- [85] H. Neuert, *Kernphysikalische Meßverfahren*, G. Braun, Karlsruhe (1966)
- [86] R.A. Forster & T.N.K. Godfrey, *MCNP – A General Monte Carlo Code for Neutron and Photon Transport. Version 3A*, ed. J.F. Briesmeister, Los Alamos, LA 739-6M, Rev. 2 (1986); J.S. Hendricks & J.F. Briesmeister, Recent MCNP Developments, *IEEE Trans. Nucl. Sci.* **39** (1992) 1035–40
- [87] A. Klett, Plutonium Detection with a New Fission Neutron Survey Meter, *IEEE Trans. Nucl. Sci.* **46** (1999) 877–9
- [88] A. Klett *et al.*, *Berthold Technologies, 3rd International Workshop on Radiation Safety of Synchrotron Radiation Sources*; RadSynch'04 SPring-8, Mikazuki, Hyogo, Japan, 17–19 November 2004
- [89] P. Marmier, *Kernphysik I*, Verlag der Fachvereine, Zürich (1977)